Modeling and Analysis of a Dual-Active-Bridge-Isolated Bidirectional DC/DC Converter to Minimize RMS Current With Whole Operating Range

Anping Tong, *Student Member, IEEE*, Lijun Hang, *Member, IEEE*, Guojie Li, *Senior Member, IEEE*, Xiuchen Jiang, and Shenyu Gao

***Abstract*—The triple phase shift (TPS) modulation scheme, which provides three control freedoms, is of great importance for the optimized operation of a dual active bridge (DAB) isolated bidirectional dc/dc converter. First of all, this paper introduces an accurate, universal model to describe the analytic expressions of the DAB converter under TPS control. Based on this, six operating modes of the DAB converter are further discussed. Afterwards, the concept of global optimal condition (GOC) equations is proposed to derive the closed form of analytic expressions of an optimal modulation scheme that makes the DAB converter operate with minimized root-mean-square (rms) current during whole power range with different operating modes. According to the GOC equations, the physical explanation of the proposed modulation scheme is further given in details, and the complex interaction among the control variables, the transferred power, and rms current is revealed. The real-time optimization process of the proposed method is also specified. Finally, the proposed methods are applied to a laboratory prototype. The experimental results confirm the theoretical analysis and practical feasibility of the proposed strategies.**

***Index Terms*—Dual-active-bridge-isolated bidirectional dc/dc converter, minimum current operation, optimal modulation scheme, triple phase shift (TPS), zero current switching.**

I. Introduction

THE dual active bridge (DAB) isolated bidirectional dc-dc converters [1], particularly which are of single phase voltage-fed full bridges with a high-frequency transformer, are popular for various applications (e.g., battery management systems, interfaces of dc distribution systems, electric vehicles, and solid state transformer) due to the advantage of galvanic isolation, soft switching characteristic without using any auxiliary element, high power density, and the ability to handle bidirectional power flow [2]–[11].

To improve the performance of DAB converters, numerous modulation schemes have been developed. The modulation schemes of DAB converters can be mainly classified into four kinds according to the control variables or the degrees of control freedom. The simplest method with only one control freedom to control the output power of DAB converters is single phase shift (SPS) modulation that controls the phase shift ratio between the primary side full bridge and the secondary side full bridge [5], [12]. For the extended phase shift (EPS) modulation scheme [13]–[16], the duty ratio of one full bridge can be adjusted additionally. Similarly, by modifying the SPS control, the dual phase shift (DPS) modulation scheme can regulate the duty ratios of both full bridges for the DAB converter with the same value [17]–[19]. Both EPS and DPS modulation schemes have two control variables. The triple phase shift (TPS) modulation scheme [5], [14], [20], [21], which controls the duty ratios of two full bridges and the phase shift ratio between them individually, facilitates the most degrees of control freedom with the constant switching frequency. Hence, the SPS control, EPS control, and the DPS control can be considered as the special cases of TPS control.

Due to the increase of control variables, the transferred power and root-mean-square (rms) value of the inductor current generated by TPS control strategy are considerably difficult to calculate. For the traditional method, researchers have to integrate the complicated current waveform piece by piece in order to obtain the analytic formulae of transferred power and rms current [14], [22], [23]. However, by that method, the physical insight of the TPS modulation scheme is not clear, and the model lacks universality. To overcome this issue and obtain a general steady-state model, the method based on the Fourier analysis is developed [24], [25]. The main disadvantage of this method is that the expressions to depict DAB converters are the sum of infinite

Manuscript received December 24, 2016; revised February 24, 2017; accepted March 23, 2017. Date of publication April 12, 2017; date of current version February 22, 2018. This work was supported in part by the Natural Science Foundation of Shanghai Science and Technology Commission under Grant 14ZR1422200, in part by the Power Electronics Science and the Education Development Program of Delta Environmental and Education Foundation under Grant DREG2015005, in part by the National Key Research and Development Program of China under Grant 2016YFB0900201, and in part by the Science Development Program of State Grid Jiangsu Electric Power Company under Grant J2017075. Recommended for publication by Associate Editor H. Li. *(Corresponding author: Lijun Hang.)*

A. Tong, L. Hang, G. Li, and X. Jiang are with the Key Laboratory of Control of Power Transmission and Conversion, Ministry of Education Shanghai Jiao Tong University, Shanghai 200240, China (e-mail: tonganping@sjtu.edu.cn; lijunhang.hhy@aliyun.com; liguojie@sjtu.edu.cn; xcjiang@sjtu.edu.cn).

S. Gao is with Nanjing Power Supply Company, State Grid Jiangsu Electric Power Company, Nanjing 210000, China (e-mail: gaosy@js.sgcc.com.cn).

Color versions of one or more of the figures in this paper are available online at http://ieeexplore.ieee.org.

Digital Object Identifier 10.1109/TPEL.2017.2692276

series. Thus, the computational effort is greatly increased due to the difficulty of dealing with the infinite series. The approximating method that only employs the fundamental component of the voltage and current is presented in [25]. However, this approximating method lacks accuracy.

In addition, since the SPS control not only results in high rms current, especially at low power level, but also prevents the converter achieving zero-voltage switching (ZVS) operation during wide power range, many research works focus on the improvement of modulation schemes which facilitate to increase the converter efficiency, to decrease the current stress, and to extend soft switching range. With the constraints of ZVS, [13] introduced a new modulation strategy based on EPS control to make DAB converters operate under soft switching in the whole operating range; however, with this strategy, the relatively large rms current, especially at lower power level, is generated. Furthermore, the strategies of DPS control to improve the efficiency of DAB converters were proposed in [18]. However, the optimized modulation schemes based on EPS control and DPS control are the local optimal solutions, which should be improved further. Since the TPS control is the unified form of these phase shift modulation schemes (i.e., SPS, DPS, EPS), the global optimal solution for all operating conditions with different power levels can be obtained by TPS control.

Due to the additional control degree of TPS control, it is considerably complex to determine the optimal modulation scheme with respect to a certain optimization objective (i.e., minimum rms current or minimum current stress). In order to solve this optimal problem, [27] and [28] employed the Lagrange multiplier method (LMM) to calculate the control variables with minimum current stress. Due to the nonconvex feasible region of this optimal problem, LMM lacks sufficiency [29]. Moreover, based on numerical solver, [21], [30], and [31] developed the modulation schemes to achieve the maximum efficiency. However, the numerical method cannot be implemented in real time for the embedded controller, and a numeric table was required by offline calculation in advance. When the parameters of DAB converter are changed, the whole numeric table has to be calculated again. Then, the difficulties are arisen for the practical application. Besides, the previous work of the optimal modulation scheme for DAB converters mainly focuses on the condition that the voltage conversion ratio $M = (n \times V_2/V_1) \leq 1$. Additionally, for the case of $M > 1$, so far no closed form of optimal modulation scheme has been proposed.

To overcome the drawback of extant methods, an analytic method to derivate the optimal modulation scheme is proposed in this paper. By analyzing the voltage waveforms of both full bridges of DAB converters and the complicated current waveform of inductor, a precise and universal model, which can be used to compute the analytic expressions to describe the converter under TPS control, is deduced. It is shown that this model can not only reduce the complexity of calculation, but also present the physical essence of the TPS modulation scheme. Therefore, six operating modes can be compartmentalized directly.

Based on this model, an optimization procedure is developed to deduce the analytic expressions of control input with the condition of minimized rms current at the given operating point. By analyzing the variation of transferred power and rms current caused by a small displacement of control coordinate, the indexes that describe the performance of each control variable are introduced. On this basis, the equations, which describe the physical properties of optimal modulation scheme, are constructed, which are referred as global optimal condition (GOC) equations in this paper. By solving the GOC equations, the analytic expressions of the optimal modulation scheme can be obtained for both $M > 1$ and $M \leq 1$ during the whole operating range. This scheme generates the minimum ohmic losses and allows a substantial improvement of the system efficiency. Comparing with the LMM and numerical method, the GOC equations facilitate in-depth physical insight of that optimal problem. Moreover, the idea of GOC equations allows researcher to freely define the objective function. The only hypothesis of this idea is that the objective function should be continuous and piecewise smooth.

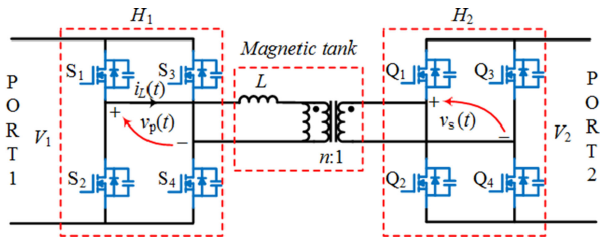

Fig. 1. Circuit schematic of the DAB converter.

This paper is further organized as follows. In Section II, the general model of the DAB converter is presented. The derivation of this model and the concise expressions of transferred power and rms current are given in detail. With the formulae deduced in Section II, the six operating modes are investigated in Section III. Subsequently, the comprehensive procedure to construct the GOC equations is shown in Section IV. The solution of GOC equations during full power range is derived to be the proposed optimized modulation scheme with respect to the minimum rms current for both cases of $M \leq 1$ and $M > 1$, and the physical explanation of this modulation scheme is demonstrated. Furthermore, the real-time optimization algorithm, which can be embedded in digital controller directly, is also detailed in this section. In Section V, the theoretic analysis and the proposed modulation schemes are verified by the experimental results obtained from a DAB converter prototype in the laboratory. Finally, Section VI presents conclusion.

II. Derivation and Analysis of the General Model of the DAB Converter

Fig. 1 shows the circuit configuration of the DAB converter that is constructed by two single-phase full bridges. These full bridge circuits (i.e., H_1 and H_2), which generate ac voltages $v_p(t)$ and $v_s(t)$, are connected by a magnetic tank that includes an inductor L and a high-frequency transformer with the turn ratio n:1. The inductance of L can be the leakage inductance of the transformer or an individual auxiliary inductor. For the convenience of analysis, PORT 1 is considered as the input, and PORT 2 is considered as the output in this paper. Hence, the power transferred from PORT 1 to PORT 2 is regarded as positive power. V_1 and V_2 denote the dc voltages of PORT 1

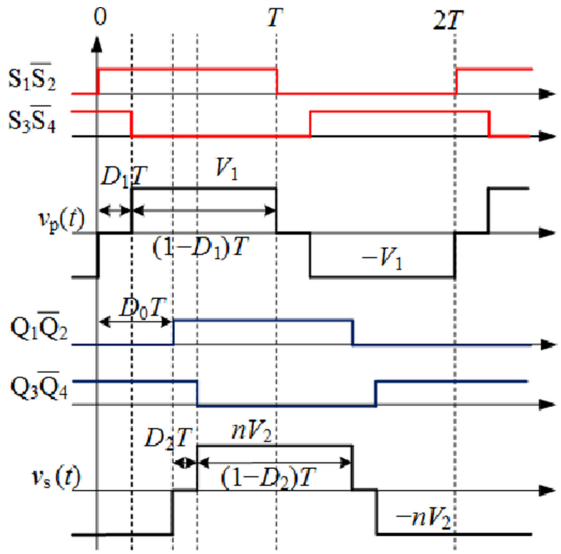

Fig. 2. Waveforms of gate driving signals and ac voltage of H_1 and H_2 for the DAB converter controlled by TPS modulation scheme.

and PORT 2, respectively. And the voltage conversion ratio M is defined as $M = (n \times V_2/V_1)$.

The typical waveforms and gate driving signals of the DAB converter controlled by the TPS modulation scheme are depicted in Fig. 2. Note that T is a half of the switching period, and the switching frequency f_s can be expressed as $f_s = 1/(2T)$. According to Fig. 2, D_1 (i.e., the phase shift ratio between S_1 and S_4) is the inner phase shift ratio of H_1, D_2 (i.e., the phase shift ratio between Q_1 and Q_4) is the inner phase shift ratio of H_2, and D_0 (i.e., the phase shift ratio between S_1 and Q_1) is the outer phase shift ratio between H_1 and H_2. All of D_0, D_1, and D_2 have the same limitation, where $D_0 \in [0,1] \wedge D_1 \in [0,1] \wedge D_2 \in [0,1]$. It is assumed that the time for S_1 turned ON is set as the beginning of the switching cycle. Then, D_1T is the time for turning ON of S_4; D_0T is the time for turning ON of Q_1, and $(D_0 + D_2)T$ is the time for turning ON of Q_4. For the TPS modulation scheme, D_0, D_1, and D_2 can be controlled independently to adjust the power P_t transferred from the input port to the output port and shape the inductor current $i_L(t)$. Then, there are three control degrees of freedom for the TPS control.

According to the gate driving signals illustrated in Fig. 2, it can be found that both $v_p(t)$ and $v_s(t)$ are three-level symmetric square waves that are generated by adjusting D_1T and D_2T. And the duty ratio of $v_p(t)$ and $v_s(t)$ is $1 - D_1$ and $1 - D_2$, respectively. Fig. 3 illustrates that this kind of three-level symmetric square waves can be composed by two two-level symmetric square waves. In Fig. 3, $S(t)$ denotes the normal two-level symmetric square wave with the period $2T$. Note that the amplitude of $S(t)$ is 0.5, and $S(t - DT)$ represents the function that is $S(t)$ with a time delay DT. Then, the sum of $S(t)$ and $S(t - DT)$ depicted in Fig. 3 is a three-level symmetric square wave with the duty ratio $1 - D$, and the amplitude of $S(t) + S(t - DT)$ is equal to 1. With a few modifications, the same results can be used to decompose $v_p(t)$ and $v_s(t)$ that are expressed as

$$\begin{cases} v_p(t) = V_1 \times [S(t) + S(t - D_1T)] \\ v_s(t) = V_2 \times [S(t - D_0T) + S(t - D_2T - D_0T)] \end{cases}. \quad (1)$$

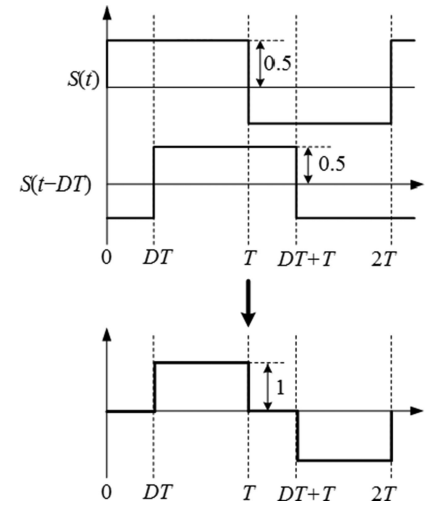

Fig. 3. Waveforms of $S(t)$, $S(t - DT)$, and $S(t) + S(t - DT)$.

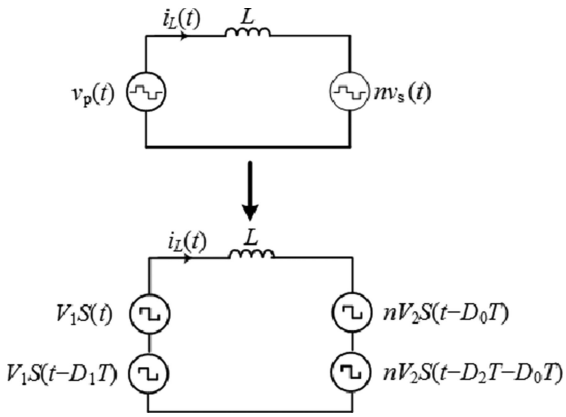

Fig. 4. Equivalent circuit of the DAB converter with TPS modulation scheme.

On the assumption of lossless component and negligible magnetizing current, the equivalent circuit of the DAB converter can be illustrated in Fig. 4 with reference to (1). As shown in Fig. 4, the primary full bridge H_1 is replaced by voltage source $v_p(t)$, and the high-frequency transformer and the secondary full bridge H_2 are replaced by the voltage source $nv_s(t)$. Based on that equivalent circuit in Fig. 4 [32], the differential equation to illustrate the dynamics of inductor current $i_L(t)$ is

$$L\frac{di_L}{dt} = (v_p(t) - nv_s(t)) = [V_1(S(t) + S(t - D_1T)) - nV_2(S(t - D_0T) + S(t - D_0T - D_2T))]. \quad (2)$$

At the steady state, it can be deduced that $i_L(t) = -i_L(t + T)$. By applying the principle of inductor volt-second balance and the linearity of integration, $i_L(t)$ is expressed as

$$i_L(t) = \frac{1}{L}[V_1(Tr(t) + Tr(t - D_1T))] - \frac{1}{L}[nV_2(Tr(t - D_0T) + Tr(t - (D_0 + D_2)T))] \quad (3)$$

where $Tr(t)$ is the symmetric triangle waveform that is the integration of $S(t)$ (i.e., $Tr(t) = \int S(t)dt$). Fig. 5 depicts the

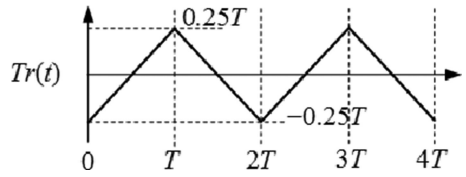

Fig. 5. Waveform of the symmetry triangle wave *Tr*(*t*).

waveform of *Tr*(*t*). Note that the amplitude of *Tr*(*t*) is 0.25*T*. Since the dc component of the inductor current $i_L(t)$ is zero at steady states, the integration of a normal two-level symmetric square wave *S*(*t*) is a bipolar triangle wave without dc component as shown in Fig. 5.

As a result, according to (3), the complicated waveform of $i_L(t)$ can be divided into four similar functions with different time delays [i.e., $Tr(t)$, $Tr(t - D_1T)$, $Tr(t - D_0T)$, and $Tr(t - (D_0 + D_2)T)$]. Comparing with the method that expresses $i_L(t)$ based on Fourier series [24], which needs to compute the infinite series, (3) describes $i_L(t)$ completely by using only four terms. Thus, the complexity of computation is reduced. Moreover, the proposed method shows more accuracy than the method of fundamental component approximation [26]. For instance, Fig. 6 illustrates the procedure of composing $i_L(t)$ by four triangle waves while the control variables are as follows: $D_0 = 0.2$, $D_1 = 0.3$, and $D_2 = 0.4$.

In consequence, the average transferred power P_t over one switching cycle 2*T* is calculated as (4), and the average rms value of inductor current $I_{\rm rms}$ is given by (5). The expanded form of (5) is composed by the term $\int Tr(t - yT) \times Tr(t - xT)dt$ that has the uniform expression as (6). By substituting (6) into (5), $I_{\rm rms}$ can be obtained directly. Neither using the detailed information of $i_L(t)$, especially the inflection point of $i_L(t)$, nor integrating $i_L(t)$ piece by piece, $I_{\rm rms}$ can be calculated. Thus, the calculation effort can be saved significantly without losing accuracy. Consequently, (4) and (5) can be the universal expressions of P_t and $I_{\rm rms}$. Therefore, the general model of the DAB converter is derived.

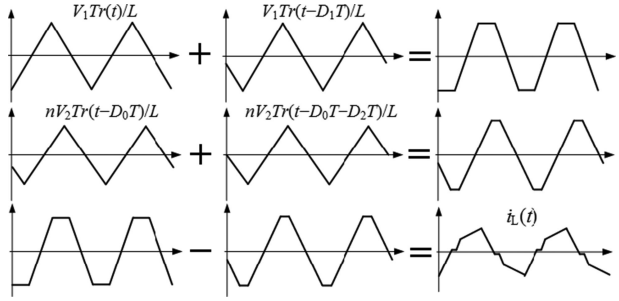

Fig. 6. Procedure of composing inductor current $i_L(t)$.

III. Analysis of Operating Modes for the DAB Converter

Due to the piecewise linearity of *Tr*(*t*), six operating modes can be compartmentalized for the whole operating range (i.e., $D_0 \in [0,1] \wedge D_1 \in [0,1] \wedge D_2 \in [0,1]$). P_t and $I_{\rm rms}$ have specific polynomials for each operating mode. To derivate the boundary of each mode, substitute (6) into (5), $I_{\rm rms}$ can be calculated as (7).

According to (7), *IA*, *IB* and *IC* are influenced by the value of control variables (i.e., D_0, D_1, and D_2). For instance, when $D_1 \le D_0$, *IA* can be written as (8). When $D_0 \le D_1$, *IA* has another form of (9): eq. (4, 5, 6, 7, 8, 9) shown at the bottom of the page.

$$P_t = \frac{1}{T}\int_0^T [v_p(t)i_L(t)dt = \frac{1}{T}\int_0^T [nv_s(t)i_L(t)dt = -\frac{nV_1V_2}{TL}\int_{D_1T}^T [Tr(t - D_0T) + Tr(t - (D_0 + D_2)T)]\,dt \tag{4}$$

$$I_{\rm rms}^2 = \frac{1}{T}\int_0^T i^2(t)dt = \frac{1}{TL^2}\int_0^T [V_1(Tr(t) + Tr(t - D_1T)) - nV_2(Tr(t - D_0T) + Tr(t - (D_0 + D_2)T))]^2 dt \tag{5}$$

$$\begin{cases} \int_0^T Tr(t - xT)Tr(t - yT)dt = \frac{1}{12}\left[0.25 - 1.5|x - y|^2 + |x - y|^3\right]T^3 & \text{for} \quad |x - y| \le 1 \\ \int_0^T Tr(t - xT)Tr(t - yT)dt = \frac{1}{12}\left[0.25 - 1.5|2 - |x - y||^2 + |2 - |x - y||^3\right]T^3 & \text{for} \quad 1 \le |x - y| \le 2 \end{cases} \tag{6}$$

$$I_{\rm rms}^2 = \frac{T^2}{6L^2}\left(\frac{1}{4}{V_1}^2 + \frac{1}{4}{V_2}^2 + \left(\frac{1}{4} - 1.5{D_1}^2 + {D_1}^3\right){V_1}^2 - \left(\frac{1}{4} - 1.5{D_0}^2 + {D_0}^3\right)V_1V_2 + \left(\frac{1}{4} - 1.5{D_2}^2 + {D_2}^3\right){V_2}^2\right)$$
$$- \frac{V_1V_2}{TL^2}\left(\underbrace{\int_0^T Tr(t - D_1T)Tr(t - D_0T)dt}_{IA} + \underbrace{\int_0^T Tr(t)Tr(t - (D_0 + D_2)T)dt}_{IB} + \underbrace{\int_0^T Tr(t - D_1T)Tr(t - (D_0 + D_2)T)dt}_{IC}\right) \tag{7}$$

$$IA = \frac{1}{12} \times \left(0.25 - 1.5(D_0 - D_1)^2 + (D_0 - D_1)^3\right)T^3V_1V_2 \ \ (\forall D_1 \le D_0) \tag{8}$$

$$IA = \frac{1}{12} \times \left(0.25 - 1.5(D_1 - D_0)^2 + (D_1 - D_0)^3\right)T^3V_1V_2 \ \ (\forall D_0 \le D_1) \tag{9}$$

TABLE I
EXPRESSIONS OF *IA*, *IB*, *IC* AT DIFFERENT CONDITIONS

Mark of term	Constraint	Expression
IA	$D_1 \le D_0$	$IA = (0.25 - 1.5(D_0 - D_1)^2 + (D_0 - D_1)^3)T^3V_1V_2/12$
IA	$D_0 \le D_1$	$IA = (0.25 - 1.5(D_1 - D_0)^2 + (D_1 - D_0)^3)T^3V_1V_2/12$
IB	$D_2 + D_0 \le 1$	$IB = (0.25 - 1.5(D_0 + D_2)^2 + (D_0 + D_2)^3)T^3V_1V_2/12$
IB	$1 \le D_2 + D_0 \le 2$	$IB = (0.25 - 1.5(2 - D_0 - D_2)^2 + (2 - D_0 - D_2)^3)T^3V_1V_2/12$
IC	$D_2 + D_0 \le D_1$	$IC = (0.25 - 1.5(D_1 - D_0 - D_2)^2 + (D_1 - D_0 - D_2)^3)T^3V_1V_2/12$
IC	$D_1 \le D_2 + D_0 \le 1 + D_1$	$IC = (0.25 - 1.5(D_0 + D_2 - D_1)^2 + (D_0 + D_2 - D_1)^3)T^3V_1V_2/12$
IC	$1 + D_1 \le D_2 + D_0 \le 2$	$IC = (0.25 - 1.5(2 - D_0 - D_2 + D_1)^2 + (2 - D_0 - D_2 + D_1)^3)T^3V_1V_2/12$

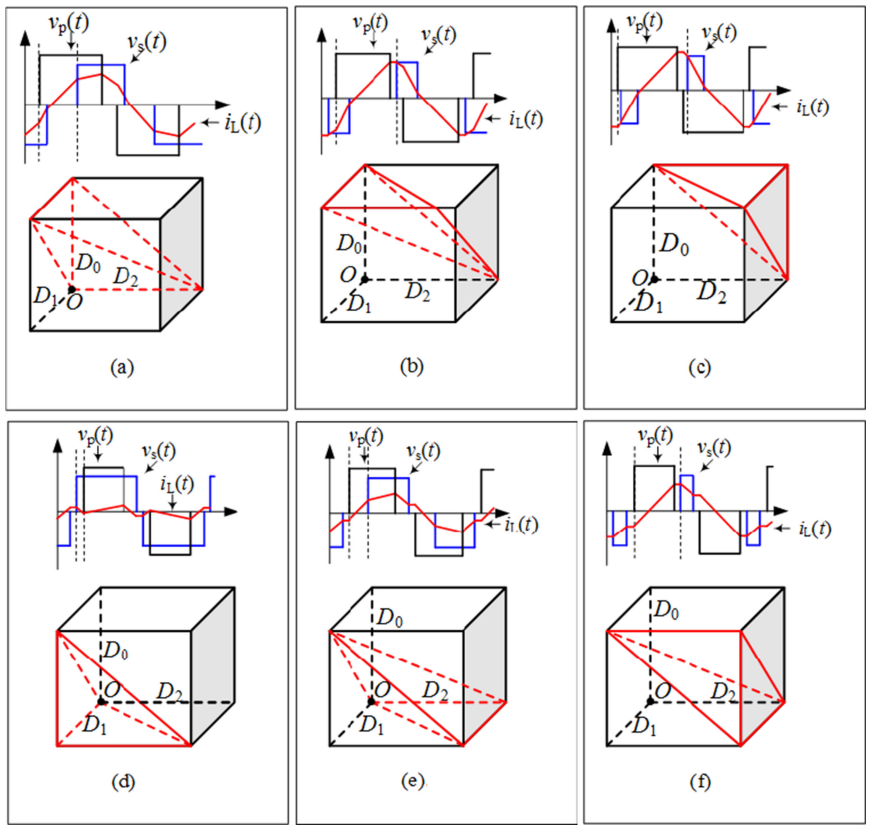

Fig. 7. Waveforms of $v_p(t)$, $v_s(t)$, and $i_L(t)$ for all operation modes and the corresponding definition domain.

The expressions of *IA*, *IB,* and *IC* at different conditions are listed in Table I. By combining the conditions of *IA*, *IB,* and *IC* terms, 12 cases can be generated. However, there are six cases with the contradictory conditions as follows:

$$\begin{cases} D_1 \le D_0 \wedge 0 \le D_0 + D_2 \le 1 \wedge 0 \le D_0 + D_2 \le D_1 \\ D_1 \le D_0 \wedge 1 \le D_0 + D_2 \le 2 \wedge 0 \le D_0 + D_2 \le D_1 \\ D_1 \le D_0 \wedge 0 \le D_0 + D_2 \le 1 \wedge 1 + D_1 \le D_0 + D_2 \le 2 \\ D_0 \le D_1 \wedge 0 \le D_0 + D_2 \le 1 \wedge 1 + D_1 \le D_0 + D_2 \le 2 \\ D_0 \le D_1 \wedge 1 \le D_0 + D_2 \le 2 \wedge 1 + D_1 \le D_0 + D_2 \le 2 \\ D_0 \le D_1 \wedge 1 \le D_0 + D_2 \le 2 \wedge 0 \le D_0 + D_2 \le D_1 \end{cases}. \tag{10}$$

Due to the contradictory conditions, these cases in (10) are not effective. Therefore, the remaining six operating modes, which can be generated by the DAB converter under TPS control, are effective and need to be further studied. Because D_0, D_1, and D_2 are the independent control variables, the definition domain of every operating mode can be depicted by a polyhedron in the three-dimensional Euclidean space. For convenience, the control input array D_0, D_1, and D_2 is represented by $D = (D_0, D_1, D_2)$ that is the coordinate in the three-dimensional Euclidean space. And $D = (D_0, D_1, D_2)$ is referred as the control coordinate. Fig. 7 depicts the typical operating waveforms for all six operating modes and its definition domain. It can be concluded that the location of $D = (D_0, D_1, D_2)$ in the space determines the sequence of the rising and falling edges of $v_p(t)$ and $v_s(t)$. For each mode, the corresponding formulae of P_t and $I_{\rm rms}$ are presented in [32].

For the reason of simplicity, normalization of P_t and $I_{\rm rms}$ can be used. Since $I_{\rm rms}$ influence the ohmic losses of the converter

TABLE II
RANGE OF $P_{n,t}$ AT EACH OPERATING MODE

Operating Mode	Lower bound of $P_{n,t}$	Upper bound of $P_{n,t}$
1	0	1
2	0	2/3
3	–0.5	0.5
4	–0.5	0.5
5	0	2/3
6	0	0.5

in the form of $R \times I_{\rm rms}^2$ and $I_{\rm rms}^2$ can be chosen as the objective function directly. And the normalization of P_t and $I_{\rm rms}^2$ is

$$P_{n,t} = P_t \Big/ \frac{nV_1V_2}{8f_sL}\ ,\ I_{2n,\rm rms} = I_{n,\rm rms}^2 = I_{\rm rms}^2 \Big/ \frac{V_1^2}{24f_s^2L^2} \quad (11)$$

where $P_{n,t}$ is the normalized value of P_t, and $I_{2n,\rm rms}$ is the normalized value of $I_{\rm rms}^2$. It is easy to find that $P_{n,t}$ is a function of control coordinate D, and $I_{2n,\rm rms}$ is a function of D and the voltage ratio $M = nV_2/V_1$. For each operating mode, the range of $P_{n,t}$ is provided in Table II.

According to Table II, the control coordinate of maximum transferred power is located in the definition domain of operating mode 1. And, $P_{n,t}$ can also be negative, which means the power is transferred from PORT 2 to PORT 1, when the DAB converter operates in mode 3 and mode 4. For mode 2, mode 3, and mode 6, $1 \le D_0 + D_2$ is met. As a result, in these three modes, when both Q_1 and Q_4 are turned ON, S_1 has been turned OFF. Therefore, the time interval satisfying $v_p(t) \times v_s(t) > 0$ does not exist, which means that the power cannot be transferred from H_1 to H_2 directly. As a consequence, the reactive power of mode 2, mode 3, and mode 6 is extremely large, which causes the significant increment of $I_{2n,\rm rms}$. For instance, Fig. 8(a) plots the key simulating waveforms of the DAB converter when it operates in mode 4 with $P_{n,t} = 0.24$ and $M = 0.5$, and as comparison, Fig. 8(b) plots the key waveforms of the DAB converter operated in mode 6 with the same conditions.

As can be observed in Fig. 8, comparing with mode 4, $I_{2n,\rm rms}$ of mode 6 is much larger for the same transferred power. For mode 2, mode 3, and mode 6, the range of $P_{n,t}$ is not extended; however, $I_{2n,\rm rms}$ is increased. Hence, these modes are not considered for the investigations to deduce the optimal modulation scheme with minimized $I_{2n,\rm rms}$.

To obtain the optimal control coordinate $D_{\rm opt} = (D_{0,\rm opt}, D_{1,\rm opt}, D_{2,\rm opt})$ with minimized $I_{2n,\rm rms}$ at given $P_{n,t}$, LMM lacks completeness. Due to the LMM's basic assumption, in which the convexity of the feasible region is needed, the solution of LMM is only of necessary conditions, but lacks of sufficiency. Fig. 9(a) depicts the set of D for $P_{n,t} = 0.2$ at mode 4, and Fig. 9(b) depicts the set of D for $P_{n,t} = 0.5$ at mode 1.

It can be seen that both of the two sets are curved surfaces that are not convex. Reference [27] presents that the optimal problem with the constrain $0 \le D_0 \le D_0 + D_2 \le D_1$ (i.e., operating mode 4) for minimizing current stress at given $P_{n,t}$ is unsolvable by using LMM. And in [28], the solution of LMM is only for local minimal current stress. So far for the case of

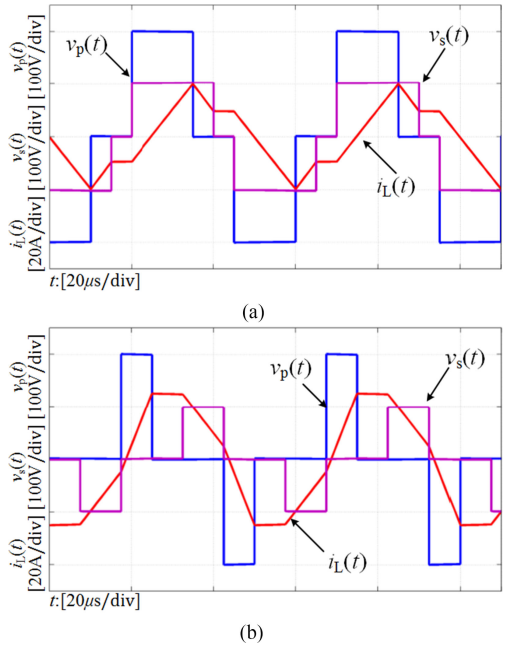

Fig. 8. Key waveforms of the DAB converter. (a) Operating in mode 4. (b) Operating in mode 6.

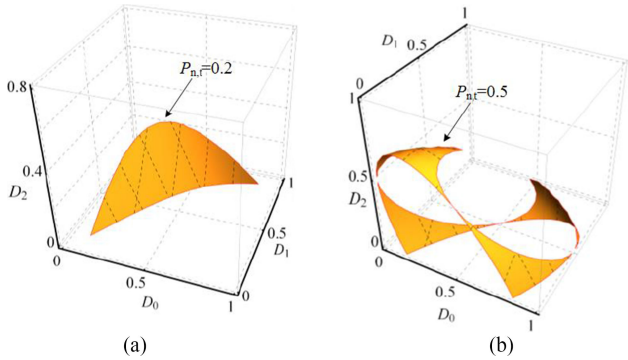

Fig. 9. Curve surface of control coordinate set. (a) Control coordinate set for $P_{n,t} = 0.2$ at mode 4. (b) Control coordinate set for $P_{n,t} = 0.5$ at mode 1.

$M > 1$, no analytic results have been proposed. To overcome the drawback of LMM and the numeric method, an analytic form of global optimized modulation scheme needs to be derived.

IV. GOC EQUATION AND THE OPTIMAL MODULATION SCHEME

A. Derivation of GOC Equations

In order to obtain the optimal control coordinate $D_{\rm opt} = (D_{0,\rm opt}, D_{1,\rm opt}, D_{2,\rm opt})$ with minimized $I_{2n,\rm rms}$ at the steady state, for the given operating point defined by the transferred power $P_{n,t}$, the GOC equations are employed [33]. For both $M \le 1$ and $M > 1$, the optimized control coordinate $D_{\rm opt} = (D_{0,\rm opt}, D_{1,\rm opt}, D_{2,\rm opt})$ is determined by GOC equations. For the reason of clarity, the below-mentioned analysis is presented mainly for the voltage ratio $M \le 1$. And for $M > 1$, the analytic expressions of $D_{\rm opt}$ is given as well.

First, the complete differentiations of P_t and $I_{2n,\mathrm{rms}}$ about D are considered

$$\Delta P_{n,t} \approx \nabla P_{n,t} \bullet (\Delta d)^T = \begin{pmatrix} \frac{\partial P_{n,t}}{\partial D_0} & \frac{\partial P_{n,t}}{\partial D_1} & \frac{\partial P_{n,t}}{\partial D_2} \end{pmatrix} \begin{pmatrix} \Delta d_0 \\ \Delta d_1 \\ \Delta d_2 \end{pmatrix}$$

$$\Delta I_{2n,\mathrm{rms}} \approx \nabla I_{2n,\mathrm{rms}} \bullet (\Delta d)^T = \begin{pmatrix} \frac{\partial I_{2n,\mathrm{rms}}}{\partial D_0} & \frac{\partial I_{2n,\mathrm{rms}}}{\partial D_0} & \frac{\partial I_{2n,\mathrm{rms}}}{\partial D_0} \end{pmatrix} \begin{pmatrix} \Delta d_0 \\ \Delta d_1 \\ \Delta d_2 \end{pmatrix} \quad (12)$$

where $D = (D_0, D_1, D_2)$ and $\Delta d = (\Delta d_0, \Delta d_1, \Delta d_2)$.

According to (12), a dimensionless parameter ξ to evaluate the performance of each control variables can be employed

$$\xi(k) = \frac{\partial I_{2n,\mathrm{rms}j}}{\partial D_k} : \frac{\partial P_{n,tj}}{\partial D_k} \quad (13)$$

where the suffix *j* represents the mark of operating modes. As mode 2, mode 3, and mode 6 are ignored, *j* can be 1, 4, and 5. *k* can be 0, 1, 2 to represent D_0, D_1, and D_2, respectively. For the given $D = (D_0, D_1, D_2)$, ξ depicts the ratio of the cost (i.e., the increment of $I_{2n,\mathrm{rms}}$) to the gain (i.e., the increment of the $P_{n,t}$) caused by a small perturbation of control variables. At an arbitrary control coordinate $D = (D_0, D_1, D_2)$ with the given voltage ratio *M*, if ξ of three control variables are not equal, for instance, $0 < \xi(1) < \xi(2)$, the following inequality can be obtained:

$$\left(\frac{\partial I_{2n,\mathrm{rms}}}{\partial D_2} : \frac{\partial P_{n,t}}{\partial D_2}\right) > \left(\frac{\partial I_{2n,\mathrm{rms}}}{\partial D_1} : \frac{\partial P_{n,t}}{\partial D_1}\right) > 0. \quad (14)$$

From (14), it is suggested that, for a given increment of $P_{n,t}$, the concomitant increment of $I_{2n,\mathrm{rms}}$ caused by adjusting D_2 is larger than that caused by adjusting D_1. It is assumed that ξ is continuous at the neighborhood of *D*, another control coordinate $D' = (D_0, D_1 + \Delta d_1, D_2 - \Delta d_2)$ at the small neighborhood of *D* can be investigated, $P_{n,t}$ and $I_{2n,\mathrm{rms}}$ of D' are

$$P_{n,t}(D') \approx P_{n,t}(D) - \frac{\partial P_{n,t}}{\partial D_2} \times \Delta d_2 + \frac{\partial P_{n,t}}{\partial D_1} \times \Delta d_1$$

$$I_{2n,\mathrm{rms}}(D') \approx I_{2n,\mathrm{rms}}(D) - \frac{\partial I_{2n,\mathrm{rms}}}{\partial D_2} \times \Delta d_2 + \frac{\partial I_{2n,\mathrm{rms}}}{\partial D_1} \times \Delta d_1. \quad (15)$$

And D' can be chosen as

$$D' = \left(D_0, D_1 + \frac{\partial P_{n,t}}{\partial D_2} \times \Delta d, D_2 - \frac{\partial P_{n,t}}{\partial D_1} \times \Delta d\right). \quad (16)$$

Then, by applying (14), we can deduce

$$P_{n,t}(D') \approx P_{n,t}(D) - \frac{\partial P_{n,t}}{\partial D_2}\frac{\partial P_{n,t}}{\partial D_1}\Delta d + \frac{\partial P_{n,t}}{\partial D_1}\frac{\partial P_{n,t}}{\partial D_2}\Delta d = P_{n,t}(D) \quad (17)$$

$$I_{2n,\mathrm{rms}}(D') \approx I_{2n,\mathrm{rms}}(D) - \frac{\partial I_{2n,\mathrm{rms}}}{\partial D_2}\frac{\partial P_{n,t}}{\partial D_1}\Delta d + \frac{\partial I_{2n,\mathrm{rms}}}{\partial D_1}\frac{\partial P_{n,t}}{\partial D_2}\Delta d \Rightarrow I_{2n,\mathrm{rms}}(D) > I_{2n,\mathrm{rms}}(D'). \quad (18)$$

This inequality (18) suggests that $I_{2n,\mathrm{rms}}$ of D' is less than $I_{2n,\mathrm{rms}}$ of *D* with the same transferred power. In terms of the optimization of loss, D' is "better" than *D*. By repeating the above-mentioned procedure to study $\xi(0)$, $\xi(1)$, and $\xi(2)$, the equations to determine the optimal control coordinate $D_{\mathrm{opt}} = (D_{0,\mathrm{opt}}, D_{1,\mathrm{opt}}, D_{2,\mathrm{opt}})$ can be obtained

$$\xi(0) = \xi(1) = \xi(2). \quad (19)$$

Because (19) characterizes the optimal control coordinate $D_{\mathrm{opt}} = (D_{0,\mathrm{opt}}, D_{1,\mathrm{opt}}, D_{2,\mathrm{opt}})$, then (19) is termed as GOC equations. Combining (19) with the equality constrains of $P_{n,t} = p$, a unique solution of $D_{\mathrm{opt}} = (D_{0,\mathrm{opt}}, D_{1,\mathrm{opt}}, D_{2,\mathrm{opt}})$ can be obtained directly [33]. Since only one weak assumption, which is the continuity of ξ, is needed, the procedure to derive the GOC (19) is effective for all the control coordinates even at the boundary of the definition domain. For the reason that the trajectory of D_{opt} is piecewise, the following discussion of D_{opt} is divided into three parts according to the power level.

B. Solution of GOC Equation at Low Power Level

According to the above-mentioned analysis, the analytic expression of $D_{\mathrm{opt}} = (D_{0,\mathrm{opt}}, D_{1,\mathrm{opt}}, D_{2,\mathrm{opt}})$ can be determined by solving (19). It can be seen that the polynomials of $P_{n,t}$ of each operating mode are not the same. Then, the specific form of GOC equations will be different for each mode. At the definition domain of mode 4, the GOC equations are expressed in the Appendix [cf., (A-1)]. With the assumption $M \leq 1$, the solution of GOC equations at mode 4 is

$$D_{0,\mathrm{opt}} = \frac{(1-M)(1-D_{1,\mathrm{opt}})}{M} \ \wedge \ D_{2,\mathrm{opt}} = 1 - \frac{1-D_{1,\mathrm{opt}}}{M} \quad (20)$$

where $D_{1,\mathrm{opt}}$ is determined by $P_{n,t}$. The definition domain of mode 4 is as follows:

$$D_0 \in [0, D_1] \ \wedge \ D_1 \in [0,1] \ \wedge \ D_2 \in [0, D_1 - D_0]. \quad (21)$$

To meet the limitation in (21), the range of $P_{n,t}$ and $D_{1,\mathrm{opt}}$ is

$$P_{n,t} \in [0, 2M(1-M)] \ \wedge \ D_{1,\mathrm{opt}} \in [1-M, 1]. \quad (22)$$

As a consequence, (20) defines the trajectory of D_{opt} at a relatively low power level, and the control coordinates that are shown in (20) can be referred as low power solution $(D_{\mathrm{opt,LPS}})$. As an example, when $P_{n,t} = 0.32$, $M = 0.8$, $V_1 = 200$ V, and $V_2 = 160$ V, Fig. 10 illustrates the typical waveforms of

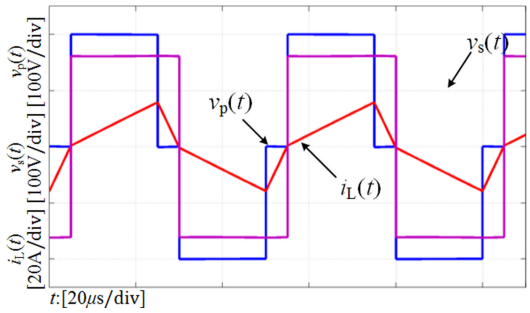

Fig. 10. Simulating waveforms of the DAB converter by control coordinate $D_{\mathrm{opt,LPS}}$ with $P_{n,t} = 0.32$ and $M = 0.8$.

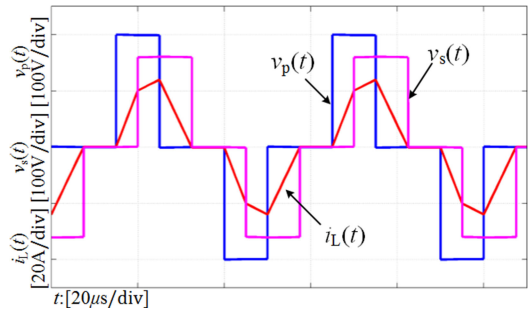

Fig. 11. Simulating waveforms of the DAB converter without negative instantaneous power.

$v_p(t)$, $v_s(t)$, and $i_L(t)$ of the DAB converter under the control of $D_{\mathrm{opt,LPS}}$.

As illustrated in Fig. 10, the shape of the inductor current $i_L(t)$ is triangular. Combining with Fig. 2, it is easy to find that $i_L(t)$ is zero at the time D_0T, D_1T, and $(D_0 + D_2)T$, with $D_{\mathrm{opt,LPS}}$ as the control input. Then, the switching devices S_3, S_4, Q_1, Q_2, Q_3, and Q_4 can achieve zero-current switching, and the switching losses can be reduced. In consequence, a remarkable improvement of efficiency for DAB converter can be accomplished.

As can be seen, since $D_{0,\mathrm{opt}} + D_{2,\mathrm{opt}} = D_{1,\mathrm{opt}}$, $D_{\mathrm{opt,LPS}}$ is located at the boundary between the definition domains for mode 4 and mode 5. Then, $D_{\mathrm{opt,LPS}}$ should be the solution of GOC equations for both mode 4 and mode 5. For mode 5, by substitution of the corresponding $P_{n,t}$ and $I_{2n,\mathrm{rms}}$ into the GOC equations [as expressed in the Appendix (A-2)], the solution is also in the form of (20). Therefore, the self-consistency of GOC equations is confirmed.

Moreover, for $D_{\mathrm{opt,LPS}}$, the instantaneous powers p_{i1} and p_{i2} generated by the full bridge H_1 and H_2 satisfy

$$\begin{cases} p_{i1}(t) = v_p(t) \times i_L(t) \geq 0 \\ p_{i2}(t) = nv_s(t) \times i_L(t) \geq 0 \end{cases}. \tag{23}$$

However, $D_{\mathrm{opt,LPS}}$ is not the only loci of the control coordinate that meets (23). In mode 5, if the control variables D_1 and D_2 satisfy the following equation [i.e., the second equation of (20)]:

$$\frac{1 - D_2}{1 - D_1} = \frac{1}{M}. \tag{24}$$

Then, (23) can also be held. In other words, (24) is the condition for control variables to eliminate negative instantaneous power. Fig. 11 plots the typical waveforms of the DAB converter, with the same condition as Fig. 10 (i.e., $P_{n,t} = 0.32$, $M = 0.8$, $V_1 = 200$ V, and $V_2 = 160$ V), controlled by another coordinates met (24). As in Fig. 11, the negative instantaneous power is also avoided; however, the rms current is relatively larger compared with Fig. 10. Fig. 12 shows the curves of $I_{2n,\mathrm{rms}}$ versus $P_{n,t}$, for different locus of control coordinates that meet the requirement of zero negative instantaneous power as (23) and (24) with $M = 0.8$.

From Fig. 12, we can conclude that the minimum $I_{2n,\mathrm{rms}}$ of a fixed $P_{n,t}$ is generated by $D_{\mathrm{opt,LPS}}$, because $D_{\mathrm{opt,LPS}}$ is

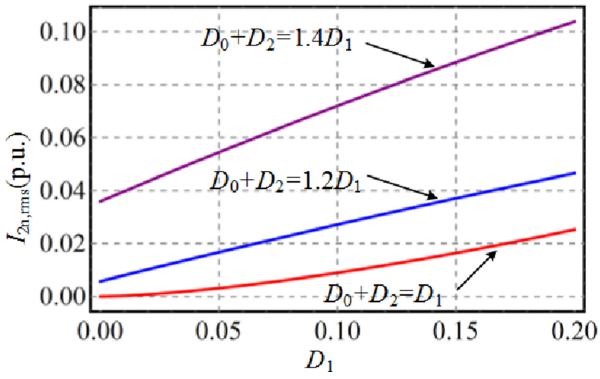

Fig. 12. $I_{2n,\mathrm{rms}}$ versus $P_{n,t}$ with different trajectories of control coordinate that avoid negative power at $M = 0.8$.

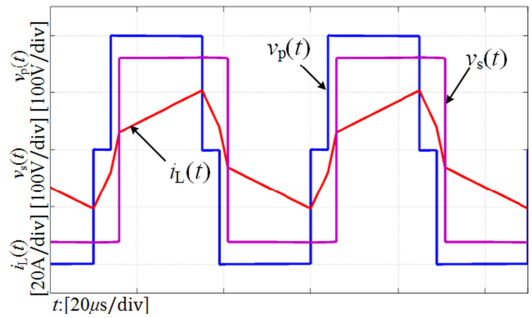

Fig. 13. Simulating waveforms of the DAB converter by control coordinate $D_{\mathrm{opt,MPS}}$ with $P_{n,t} = 0.5$ and $M = 0.8$.

the unique solution to meet the requirement of zero negative instantaneous power and $D_0 + D_2 = D_1$ simultaneously.

C. Solution of GOC Equation at Medium Power Level

For the case that the transferred power exceeded the limitation of $D_{\mathrm{opt,LPS}}$ (22), the GOC equations can be solved by using the formulae of $P_{n,t}$ and $I_{2n,\mathrm{rms}}$ in mode 1. For $M \leq 1$, the expressions of D_{opt} at medium power level are as follows:

$$\begin{aligned} D_{0,\mathrm{opt}} &= \frac{D_{1,\mathrm{opt}} - 1 + M + D_{1,\mathrm{opt}}M}{2M} \\ &\quad + \frac{\sqrt{(D_{1,\mathrm{opt}} - 1)^2 + M^2(D_{1,\mathrm{opt}}^2 - 1)}}{2M} \\ D_{2,\mathrm{opt}} &= 0. \end{aligned} \tag{25}$$

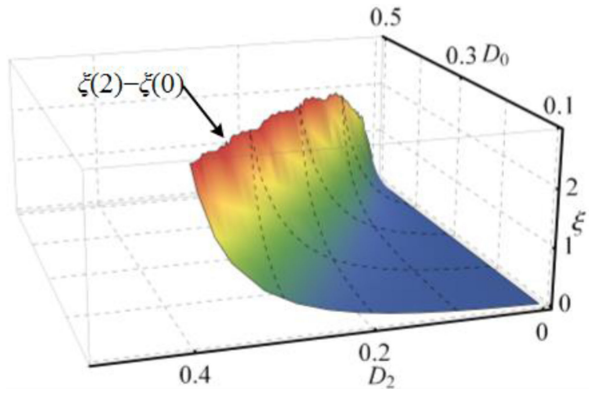

Fig. 14. Curve surface of $\xi(2) - \xi(0)$ at mode 1.

Due to the constrains of the definition domain of mode 1 (i.e., $D_1 \leq D_0$), the limitations of $P_{n,t}$ and D_1 are

$$P_{n,t} \in \left[2M(1-M), \frac{2(M^2-1+\sqrt{1-M^2})}{M^2}\right] \wedge D_1 \in [0, 1-M]\,. \tag{26}$$

Then, the solution of (25) is effective at the medium power level. For this reason, (25) can be named as medium power solution $(D_{\text{opt,MPS}})$. So far the concise expressions of $D_{\text{opt,MPS}}$ and the corresponding $P_{n,t}$ has not been clearly dealt with in extant research works. As an example, Fig. 13 illustrates the typical waveforms of the DAB converter controlled by $D_{\text{opt,MPS}}$, at $P_{n,t} = 0.5$, $M = 0.8$, $V_1 = 200$ V, and $V_2 = 160$ V.

Comparing with the typical waveforms of DAB controlled by $D_{\text{opt,LPS}}$ illustrated in Fig. 10, the negative instantaneous power is unavoidable. In Fig. 13, the time interval for $v_p(t) \times i_L(t) < 0$ shows that the amount of negative instantaneous power is relatively small. According to (25), the control variable D_2 is equal to zero in the case of medium power level. This is caused by the following inequality in mode 1:

$$\xi(2) > \xi(1) \wedge \xi(2) > \xi(0) \quad \forall D_2 \neq 0\,. \tag{27}$$

For instance, Fig. 14 plots $\xi(2) - \xi(0)$ at mode 1 when $D_1 = 0.1$ and $M = 0.8$. As can be seen, $\xi(2) - \xi(0)$ is larger than zero when $D_2 \neq 0$. Therefore, to reduce $I_{2n,\text{rms}}$, D_2 should be zero at mode 1 with $M \leq 1$. When D_2 equals to zero, the curves of $I_{2n,\text{rms}}$ versus D_1 are depicted in Fig. 15. With the given $P_{n,t}$, Fig. 15 shows that $I_{2n,\text{rms}}$ can achieve the minimum value when the control coordinate D meets (25).

D. Solution of GOC Equation at High Power Level

When the transferred power $P_{n,t}$ is even higher than the upper limitation of $D_{\text{opt,MPS}}$ as (26), the solution of GOC equations is also located in mode 1. However, the expressions of GOC equations at mode 1 for the high power level are

$$D_{1,\text{opt}} = 0 \ \wedge \ D_{2,\text{opt}} = 0. \tag{28}$$

Correspondingly, $P_{n,t}$ and D_0 should satisfy (29). Hence, the control coordinate determined by (28) is termed as high power solution $(D_{\text{opt,HPS}})$. As mentioned before, D_2 should be equal to zero at mode 1. And Fig. 16 illustrates the curves of $I_{2n,\text{rms}}$

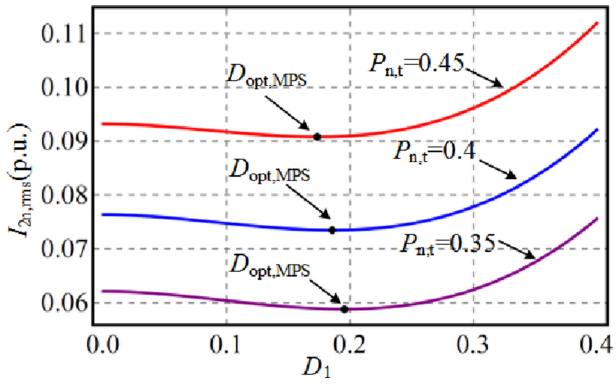

Fig. 15. $I_{2n,\text{rms}}$ versus D_1 with different $P_{n,t}$ at medium power level.

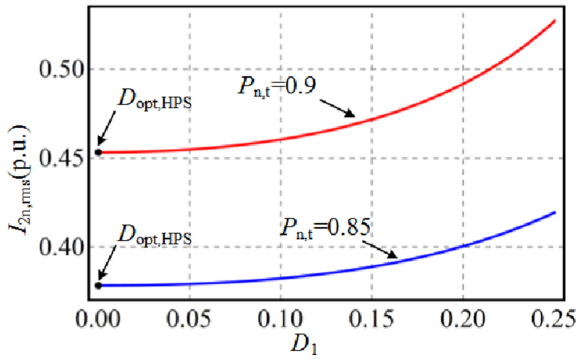

Fig. 16. $I_{2n,\text{rms}}$ versus D_1 with different $P_{n,t}$ at high power level.

versus D_1 with $D_2 = 0$ and $M = 0.8$ at high power level

$$P_{n,t} \in \left[\frac{2(M^2-1+\sqrt{1-M^2})}{M^2}, 1\right]$$
$$D_0 \in \left[\frac{-1+M+\sqrt{1-M^2}}{2M}, \frac{1}{2}\right]. \tag{29}$$

Fig. 16 demonstrates that $I_{2n,\text{rms}}$ can achieve the minimum value at $D_1 = 0$ for high power level. In conclusion, at high power level, the minimum current of $I_{2n,\text{rms}}$ for the given $P_{n,t}$ is generated by the SPS modulation scheme.

From Sections IV-B to IV-D, combining with (20), (25), and (28), the closed form of the control coordinate D_{opt}, which is used to minimize $I_{2n,\text{rms}}$ at given $P_{n,t}$ and M during the whole operating range, can be obtained. It can be verified that the numeric results obtained by offline computation precisely meet the results calculated by D_{opt}. Therefore, the theoretical analysis of D_{opt} is proved. The trajectories of the optimal control variables D_{opt} versus $P_{n,t}$ are depicted in Fig. 17 at $M = 0.8$.

From Fig. 17, it is revealed that the control variables transfer from the low power level to the medium power level, then to the high power level, seamlessly. Moreover, the respective ranges of $P_{n,t}$ for $D_{\text{opt,LPS}}$, $D_{\text{opt,MPS}}$, and $D_{\text{opt,HPS}}$ cover the whole power range (i.e., $P_{n,t} \in [0, 1]$) of the DAB converter without overlapping or vacancy. The respective range of $P_{n,t}$ for $D_{\text{opt,LPS}}$, $D_{\text{opt,MPS}}$, and $D_{\text{opt,HPS}}$ is changed with the voltage transfer ratio M, which is depicted in Fig. 18.

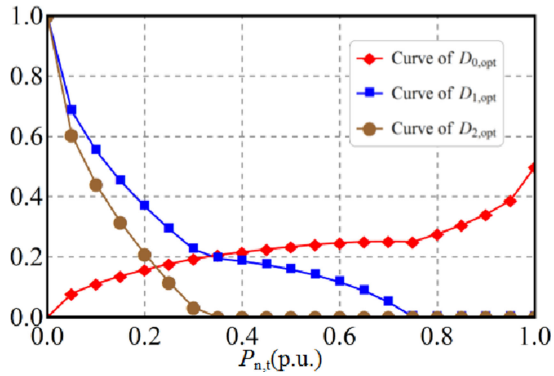

Fig. 17. Control variables (i.e., D_0, D_1, D_2) versus $P_{n,t}$ with $M = 0.8$.

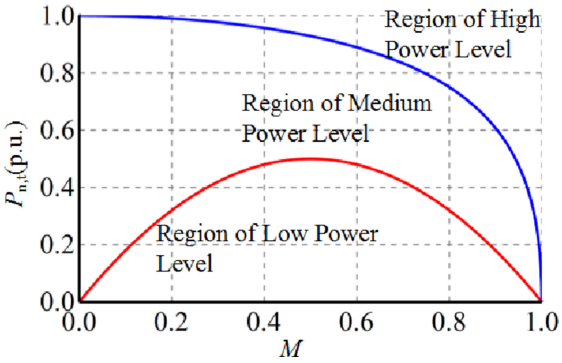

Fig. 18. Range of low power level, medium power level, and high power level for $M < 1$.

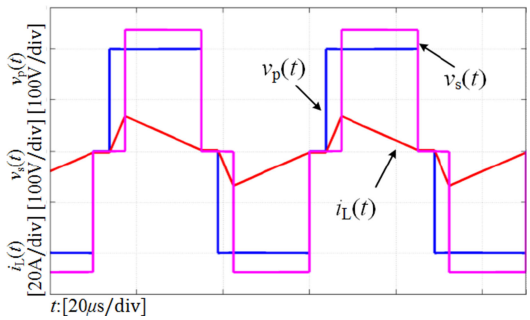

Fig. 19. Simulating waveforms of the DAB converter by control coordinate $D_{\mathrm{opt,LPS}}$ with $P_{n,t} = 0.2$ and $M = 1.2$.

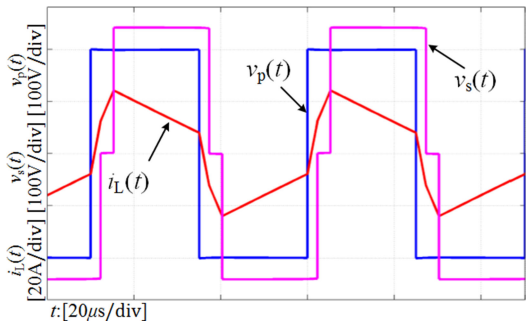

Fig. 20. Simulating waveforms of the DAB converter by control coordinate $D_{\mathrm{opt,MPS}}$ with $P_{n,t} = 0.5$ and $M = 1.2$.

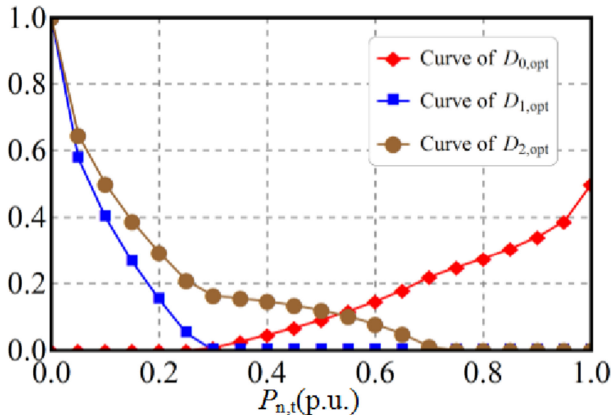

Fig. 21. Control variables (i.e., D_0, D_1, D_2) versus $P_{n,t}$ with $M = 1.2$.

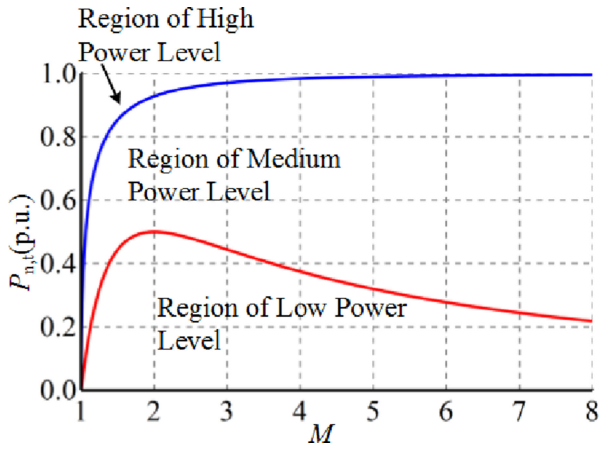

Fig. 22. Range of low power level, medium power level, and high power level for $M > 1$.

E. Solution of GOC Equation for M > 1

For the extant publications on DAB optimal modulation scheme, the case of $M > 1$ is not considered [21], [27], [28], [34]. However, the limitation of $P_{n,t}$ of D_{opt} [i.e., (22), (26), and (29)] includes the terms of $(1 - M)$ and $\sqrt{1 - M}$ that are not effective for $M > 1$. Note that the inverse power flow that is transferred from PORT 2 to PORT 1 with $M \leq 1$ is equal to the positive power flow from PORT 1 to PORT 2 with $M > 1$. Therefore, the optimized modulation scheme for $M > 1$ should be discussed further.

In terms of the derivation of GOC equations, it can be concluded that the optimized control coordinate with respect to the minimum $I_{2n,\mathrm{rms}}$ with $M > 1$ meets the constraints of GOC equations as well. As a result, the closed form of optimized control coordinate with $M > 1$ can be obtained by solving GOC equation [cf., (A-1)–(A-3)].

As can be found, (A-1) does not have effective solution with $M > 1$. In consequence, the optimal control coordinate does not locate in the definition domain of mode 4. By solving (A-2) for the case of $M > 1$, the expressions of D_{opt} at low power level are

$$D_{0,\mathrm{opt}} = 0 \ \wedge \ D_{1,\mathrm{opt}} = 1 + MD_{2,\mathrm{opt}} - M \qquad (30)$$

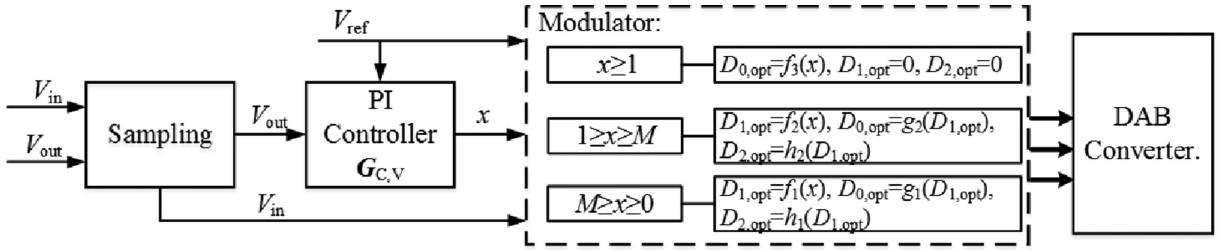

Fig. 23. Control structure of close loop for the DAB converter with the online optimization algorithm.

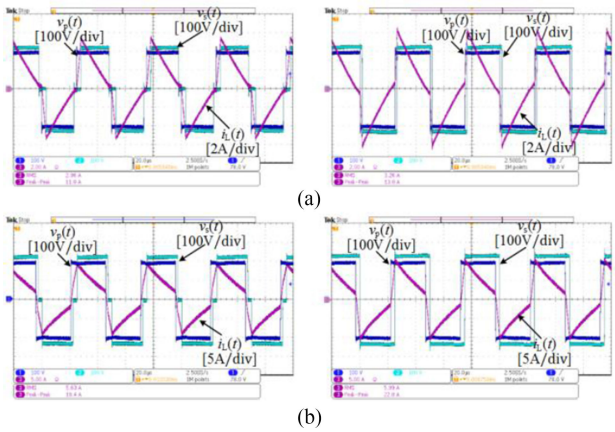

Fig. 24. Experimental waveforms at $V_2 = 230$ V ($M = 1.15$). (a) $P_t = 540$ W. (b) $P_t = 1080$ W.

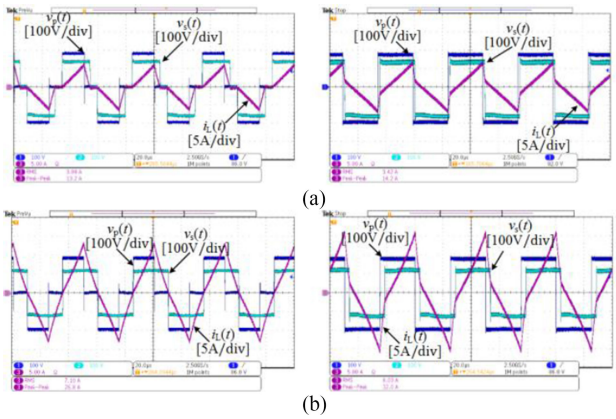

Fig. 25. Experimental waveforms at $V_2 = 160$ V ($M = 0.8$). (a) $P_t = 400$ W. (b) $P_t = 900$ W.

where $D_{2,\text{opt}}$ is determined by $P_{n,t}$. To meet the constrains of the definition domain of mode 5 (i.e., $0 \leq D_1 \leq D_2 + D_0 \leq 1$), the limitations of $P_{n,t}$ and D_2 are

$$P_{n,t} \in \left[0, \frac{2}{M^2}(M-1)\right] \wedge D_2 \in \left[\frac{M-1}{M}, 1\right]. \quad (31)$$

Similarly, D_{opt} determined by (30) is termed as $D_{\text{opt,LPS}}$. As an example, Fig. 19 illustrates the typical waveforms of $v_p(t)$, $v_s(t)$, and $i_L(t)$ of the DAB converter controlled by $D_{\text{opt,LPS}}$ as (30) with $P_{n,t} = 0.2$, $M = 1.2$, $V_1 = 200$ V, and $V_2 = 240$ V. As in Fig. 20, $D_{\text{opt,LPS}}$ derived from (30) also eliminate the negative instantaneous power with $M > 1$ as well. For the medium power level, the solution of GOC equation [i.e., (A-3)] is

$$\begin{aligned} D_{0,\text{opt}} &= \frac{1 - D_{2,\text{opt}} - M + MD_{2,\text{opt}}}{2} \\ &\quad + \frac{\sqrt{D_{2,\text{opt}}^2 - 1 + M^2(1 - D_{2,\text{opt}})^2}}{2} \\ D_{1,\text{opt}} &= 0. \end{aligned} \quad (32)$$

The corresponding $P_{n,t}$ and D_2 for (32) are

$$\begin{aligned} P_{n,t} &\in \left[\frac{2}{M^2}(M-1), 2\left(1 - M^2 + M\sqrt{M^2-1}\right)\right] \\ D_2 &\in \left[0, \frac{M-1}{M}\right]. \end{aligned} \quad (33)$$

Condition (32) can be referred as $D_{\text{opt,MPS}}$. For instance, Fig. 20 plots the key waveforms of the DAB converter controlled by $D_{\text{opt,MPS}}$ with $P_{n,t} = 0.5$, $M = 1.2$, $V_1 = 200$ V, and $V_2 = 240$ V.

Furthermore, for the transferred power higher than the upper limit of (33), the effective solution of GOC equation is

$$D_{1,\text{opt}} = 0 \wedge D_{2,\text{opt}} = 0. \quad (34)$$

According to (34), the SPS modulation scheme can generate the minimum $I_{2n,\text{rms}}$ even with $M > 1$ at high power level. And the corresponding ranges of $P_{n,t}$ and D_0 are expressed in (35). As a conclusion, the trajectories of the control variables (i.e., D_0, D_1, and D_2) versus $P_{n,t}$ are depicted in Fig. 21 at $M = 1.2$. The respective range of $P_{n,t}$ for $D_{\text{opt,LPS}}$, $D_{\text{opt,MPS}}$, and $D_{\text{opt,HPS}}$ with $M > 1$ versus M is depicted in Fig. 22

$$\begin{aligned} P_{n,t} &\in \left[2\left(1 - M^2 + M\sqrt{M^2-1}\right), 1\right] \\ D_0 &\in \left[\frac{1 - M + \sqrt{M^2-1}}{2}, \frac{1}{2}\right]. \end{aligned} \quad (35)$$

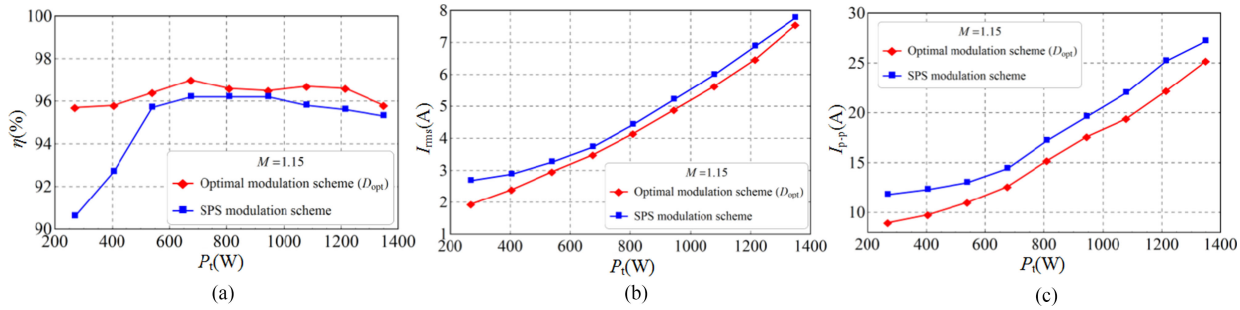

Fig. 26. Experimental curves with $V_2 = 230$ V $(M = 1.15)$ at different transferred powers. (a) Efficiency. (b) RMS current. (c) Peak–peak current.

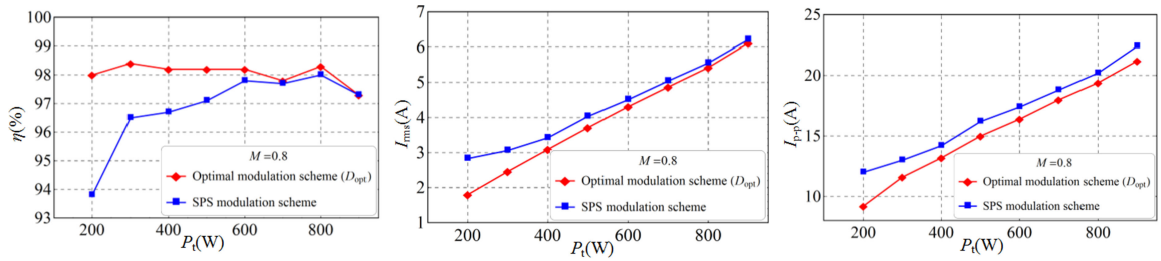

Fig. 27. Experimental curves with $V_2 = 160$ V $(M = 0.8)$ at different transferred powers. (a) Efficiency. (b) RMS current. (c) Peak–peak current.

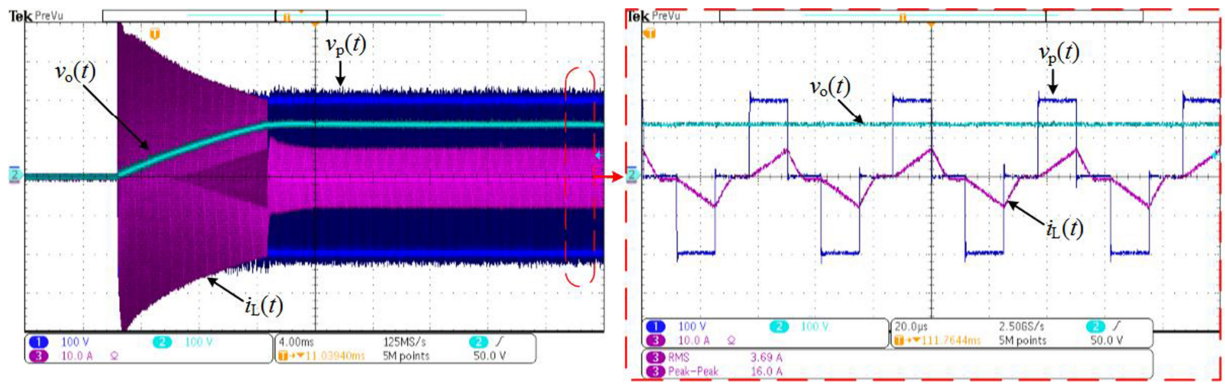

Fig. 28. Experimental waveforms of closed loop implementation: start-up response.

F. Close Loop Control Structure for the Proposed Controller and Real-Time Optimization

Fig. 23 illustrates the control structure for an online optimization algorithm when the DAB converter operates at $M \leq 1$ with the close loop system. The proposed algorithm can be employed in embedded processor (e.g., DSP) without numeric table.

As an example, a single close loop voltage controller is employed to regulate the output voltage, and x denotes the output of the voltage controller. In Fig. 23, the proposed optimal modulation strategy is embedded in the modulator that transforms the output of controller x into the optimal control coordinate D_{opt}. Note the voltage conversion ratio M, for online implementation, is calculated by $M = (nV_{\text{ref}}/V_1)$ [27].

In addition, it should be pointed that the functions $g_1(\cdot)$, $g_2(\cdot)$, $h_1(\cdot)$, $h_2(\cdot)$ can be constructed according to (20) and (25) at $M \leq 1$. $f_1(\cdot)$, $f_2(\cdot)$, $f_3(\cdot)$ are utilized to determine the function between x and D_{opt}, these functions can be constructed as follows:

$$\begin{aligned} f_1(x) &= 1 - x \\ f_2(x) &= 1 - x \\ f_3(x) &= \frac{1}{2M} \times \left[(2x - 3) \times \left(1 - \sqrt{1 - M^2}\right) + M\right]. \end{aligned} \tag{36}$$

In accordance with (36), the output of controller x is limited to $x \in [0, 1.5]$. By modifying the parameters and functions of the modulator according to (30) and (32), the control diagram can be used for the case of $M > 1$. According to Fig. 23, the proposed optimization controller is easy to be implemented in a real-time controller.

TABLE III
CIRCUIT PARAMETERS OF THE PROTOTYPE

Items	Descriptions	Specifications
V_1	Input Voltage	200 V
V_2	Output Voltage	230 V, 160 V
f_s	Switching Frequency	20 kHz
L	Auxiliary Inductor	105.2 μH
	Magnetic Material	Sendust Alloy
n	Turn Ratio	1:1
	Magnetic Material	Ferrite

V. EXPERIMENTAL RESULTS

A prototype of the DAB converter, with the specifications listed in Table III, was built in the laboratory. And the theoretic analysis of the previous sections has been verified in experiment. The converter is built by SiC MOSFET (i.e., C3M0065090D), and individual antiparallel diodes, in particular SiC Schottky diode (i.e., C3D08060A), are used. The proposed control strategy is implemented in a digital signal processor (i.e., TMS320F28335) that is employed to generate the gate driving signals. The input voltage V_1 is fixed at 200 V. In order to test the proposed modulation schemes at different voltage conversion ratio conditions for both $M > 1$ and $M \leq 1$, V_2 are set at different values. For instance, the experimental waveforms with the output voltage $V_2 = 230$ and 160 V are given to demonstrate the theoretical analysis. For $V_2 = 230$ V, Fig. 24(a) illustrates the operating waveforms for low power level with $P_t = 540$ W, and Fig. 24(b) illustrates the operating waveforms for medium power level with $P_t = 1080$ W. For $V_2 = 160$ V, Fig. 25(a) illustrates the operating waveforms for low power level with $P_t = 400$ W, and Fig. 25(b) illustrates the operating waveforms for medium power level with $P_t = 900$ W.

As a comparison, both the waveforms controlled by the optimal modulation scheme (i.e., the left subplot) and the SPS modulation scheme (i.e., the right subplot) are shown in each subplot of Figs. 24 and 25.

As observed, the rms value and the peak–peak value of inductor current are reduced significantly by the optimal modulation scheme. From the experimental results, for instance, at $V_2 = 160$ V [cf., Fig. 25(a)] and the transferred power 400 W, the measured rms current decreases from 3.42 A by SPS control to 3.09 A by the proposed optimal control; the peak–peak current decreases from 14.2 A by SPS control to 13.2 A by the optimal control; and the efficiency increases from 96.7% by SPS control to 98.2% by the optimal control. The peak–peak current, rms current, and efficiency curves for different selected operating points, which are defined by the transferred power P_t and output voltage V_2, are depicted in Figs. 26, and 27. The blue lines mark the optimal modulation scheme, and the red lines mark the SPS modulations scheme. Since the performance improvement offered by the optimal modulation scheme is more significant at low power level and medium power level, the related results till 50% of maximum transferred power (i.e., $P_{n,t} = 0.5$) are compared for both $M > 1$ and $M \leq 1$.

As can be seen, a remarkable performance improvement of the DAB converter can be accomplished by the proposed optimized modulation scheme $(D_{\rm opt})$ especially at low power level. Since the parasitic capacitor of the SiC MOSFET (C3M0065090D) is relatively small, the ohmic losses caused by the rms current are the dominant component of whole losses, the efficiency of the DAB converter is of significant improvement by using the optimal modulation scheme.

The experimental results for online optimization are depicted in Fig. 28 with the control algorithm shown in Fig. 19 and (36). The input and output voltages are 200 V and 140 V, respectively. And the load resistance is 46.2 Ω. In order to reduce the current overshoot, the controller output x is limited in the range [0,1] for start-up. As can be observed, the optimized control is achieved by the proposed control algorithm at the steady state.

VI. CONCLUSION

This paper has detailed a novel model with high accuracy and good universality to depict the DAB converter controller by the TPS modulation scheme. The complicated inductor current can be separated into four similar triangle waves on the assumption of lossless components and negligible magnetizing current as the steady state. Thereby, the general expressions of transferred power and rms current can be obtained. Based on the formula of rms current, the six operating modes can be compartmentalized directly. And the performance of each operating mode is also evaluated in this paper.

After that, to overcome the drawback of LMM and numerical method, a general procedure, which is effective for the whole operating range with both $M \leq 1$ and $M > 1$, for the derivation of the optimized modulation scheme is presented. By considering the variation of transferred power and rms current with small displacement of control coordinate, the indexes to assess each control variable are obtained. Hence, the equations, named GOC equations, to derive the optimized modulation scheme with respect to the minimum rms current can be constructed by these indexes. Therefore, the analytic expressions of the optimal control coordinate are obtained. As a consequence, the minimum ohmic losses can be achieved. Based on the optimized modulation scheme, the real-time optimization algorithm that can be embedded in a digital controller directly is given.

Finally, the theoretical analysis and proposed control strategies are verified by a laboratory prototype with several M (i.e., $M = 0.8$ and 1.15). The proposed control strategies are successfully implemented on the prototype converter, yielding significant improvement of efficiency (peak efficiency is higher than 98%).

As can be seen, a remarkable performance improvement of the DAB converter can be accomplished by the proposed optimized modulation scheme $(D_{\rm opt})$ especially at low power level. Since the parasitic capacitor of the SiC MOSFET (C3M0065090D) is relatively small, the ohmic losses caused by the rms current are the dominant component of whole losses, the efficiency of the DAB converter is of significant improvement by using the optimal modulation scheme.

APPENDIX

The GOC equations of mode 4, mode 5, and mode 1 are, respectively, eq. (A-1, A-2, A-3) shown at top of the next page.

$$\frac{\left(-1.5D_1^2-3D_0(1-D_1)-1.5D_2+1.5D_1(1+D_2)\right)\times M}{D_1-1}$$
$$=\frac{\left(3D_0^2+(1.5+1.5D_2)D_2+D_0(3+3D_2)\right)\times M+D_1^2(-1.5+3M)+\left(1.5+(-3-6D_0-3D_2)\right)D_1M}{2\times(0.5+D_0-D_1+0.5D_2)}$$
$$=\frac{\left(-1.5D_1^2+3D_0(D_1-1)+D_1(1.5+3D_2)+D_2(-3+1.5M-1.5MD_2)\right)M}{D_1-1} \tag{A-1}$$

$$\frac{\left(1.5D_0^2+1.5D_1(1-D_2)-1.5D_2(1-D_2)-3D_0(1-D_2)\right)\times M}{D_0+D_2-1}$$
$$=\frac{1.5D_1^2+\left(1.5D_2(-1+D_2)+3D_0(-1+D_2)\right)\times M+D_1\left(-1.5+(3-3D_2)\times M\right)}{D_2-1}$$
$$=\frac{1.5M\times\left(D_0^2+0.5D_1^2+D_1(0.5-D_2)+D_0(-1-D_1+2D_2)+D_2(-1+D_2+0.5M-0.5D_2M\right)}{-0.5+D_0-0.5D_1+D_2} \tag{A-2}$$

$$\frac{\left(1.5D_0^2+0.75D_1^2+0.75D_1(1-D_2)+0.75D_2(-1+D_2)+1.5D_0(-1-D_1+D_2)\right)\times M}{-0.5+D_0-0.5D_1+D_2}$$
$$=\frac{\left(3D_0^2-1.5D_2(1-D_2)+3D_0(-1+D_2)\right)\times M+D_1^2(1.5+3M)+D_1\left(-1.5+(3-6D_0-3D_2)M\right)}{2\times(-0.5+D_0-0.5D_1+D_2)}$$
$$=\frac{1.5M\times\left(D_0^2+0.5D_1^2+D_1(0.5-D_2)+D_0(-1-D_1+2D_2)+D_2(-1+D_2+0.5M-0.5D_2M\right)}{-0.5+D_0-0.5D_1+D_2} \tag{A-3}$$

REFERENCES

[1] M. N. Kheraluwala, R. W. Gascoigne, D. M. Divan, and E. D. Baumann, "Performance characterization of a high-power dual active bridge dc-to-dc converter," *IEEE Trans. Ind. Appl.*, vol. 28, no. 6, pp. 1294–1301, Nov. 1992.

[2] S. Inoue and H. Akagi, "A bidirectional isolated dc-dc converter as a core circuit of the next-generation medium-voltage power conversion system," *IEEE Trans. Power Electron.*, vol. 22, no. 2, pp. 535–542, Mar. 2007.

[3] B. Zhao, Q. Song, W. Liu, and Y. Sun, "Overview of dual-active-bridge isolated bidirectional dc-dc converter for high-frequency-link power-conversion system," *IEEE Trans. Power Electron.*, vol. 29, no. 8, pp. 4091–4106, Aug. 2014.

[4] X. She, X. Yu, F. Wang, and A. Q. Huang, "Design and demonstration of a 3.6-kV-120-V/10-kVA solid-state transformer for smart grid application," *IEEE Trans. Power Electron.*, vol. 29, no. 8, pp. 3982–3996, Aug. 2014.

[5] F. Krismer and J. W. Kolar, "Accurate small-signal model for the digital control of an automotive bidirectional dual active bridge," *IEEE Trans. Power Electron.*, vol. 24, no. 12, pp. 2756–2768, Dec. 2009.

[6] N. M. L. Tan, T. Abe, and H. Akagi, "Design and performance of a bidirectional isolated dc-dc converter for a battery energy storage system," *IEEE Trans. Power Electron.*, vol. 27, no. 3, pp. 1237–1248, Mar. 2012.

[7] Y. Shi, R. Li, Y. Xue, and H. Li, "Optimized operation of current-fed dual active bridge dc/dc converter for PV applications," *IEEE Trans. Ind. Electron.*, vol. 62, no. 11, pp. 6986–6995, Nov. 2015.

[8] B. Zhao, Q. Song, W. Liu, and Y. Xiao, "Next-generation multi-functional modular intelligent UPS system for smart grid," *IEEE Trans. Ind. Electron.*, vol. 60, no. 9, pp. 3602–3618, Sep. 2013.

[9] F. Krismer and J. W. Kolar, "Accurate power loss model derivation of a high-current dual active bridge converter for an automotive application," *IEEE Trans. Ind. Electron.*, vol. 57, no. 3, pp. 881–891, Mar. 2010.

[10] J. Ge, Z. Zhao, L. Yuan, and T. Lu, "Energy feed-forward and direct feed-forward control for solid-state transformer," *IEEE Trans. Power Electron.*, vol. 30, no. 8, pp. 4042–4047, Aug. 2015.

[11] Y. Shi, R. Li, Y. Xue, and H. Li, "High-frequency-link-based grid-tied PV system with small dc-link capacitor and low-frequency ripple-free maximum power point tracking," *IEEE Trans. Power Electron.*, vol. 31, no. 1, pp. 328–339, Jan. 2016.

[12] H. Bai, C. Mi, C. Wang, and S. Gargies, "The dynamic model and hybrid phase-shift control of a dual-active-bridge converter," in *Proc. 34th Annu. Conf. IEEE Ind. Electron.*, 2008, pp. 2840–2845.

[13] G. G. Oggier, G. O. Garcia, and A. R. Oliva, "Modulation strategy to operate the dual active bridge dc-dc converter under soft switching in the whole operating range," *IEEE Trans. Power Electron.*, vol. 26, no. 4, pp. 1228–1236, Apr. 2011.

[14] A. K. Jain and R. Ayyanar, "Pwm control of dual active bridge: Comprehensive analysis and experimental verification," *IEEE Trans. Power Electron.*, vol. 26, no. 4, pp. 1215–1227, Apr. 2011.

[15] B. Zhao, Q. Yu, and W. Sun, "Extended-phase-shift control of isolated bidirectional dc-dc converter for power distribution in microgrid," *IEEE Trans. Power Electron.*, vol. 27, no. 11, pp. 4667–4680, Nov. 2012.

[16] G. G. Oggier, G. O. GarcÍa, and A. R. Oliva, "Switching control strategy to minimize dual active bridge converter losses," *IEEE Trans. Power Electron.*, vol. 24, no. 7, pp. 1826–1838, Jul. 2009.

[17] H. Bai and C. Mi, "Eliminate reactive power and increase system efficiency of isolated bidirectional dual-active-bridge dc–dc converters using novel dual-phase-shift control," *IEEE Trans. Power Electron.*, vol. 23, no. 6, pp. 2905–2914, Nov. 2008.

[18] B. Zhao, Q. Song, and W. Liu, "Efficiency characterization and optimization of isolated bidirectional dc/dc converter based on dual-phase-shift control for dc distribution application," *IEEE Trans. Power Electron.*, vol. 28, no. 4, pp. 1711–1727, Apr. 2013.

[19] B. Zhao, Q. Song, W. Liu, and W. Sun, "Current-stress-optimized switching strategy of isolated bidirectional dc/dc converter with dual-phase-shift control," *IEEE Trans. Ind. Electron.*, vol. 60, no. 10, pp. 4458–4467, Oct. 2013.

[20] K. Wu, C. W. de Silva, and W. G. Dunford, "Stability analysis of isolated bidirectional dual active full-bridge dc-dc converter with triple phase-shift control," *IEEE Trans. Power Electron.*, vol. 27, no. 4, pp. 2007–2017, Apr. 2012.

[21] F. Krismer and J. W. Kolar, "Closed form solution for minimum conduction loss modulation of DAB converters," *IEEE Trans. Power Electron.*, vol. 27, no. 1, pp. 174–188, Jan. 2012.

[22] Y. Xie, J. Sun, and J. S. Freudenberg, "Power flow characterization of a bidirectional galvanically isolated high-power dc/dc converter over a wide operating range," *IEEE Trans. Power Electron.*, vol. 25, no. 1, pp. 54–66, Jan. 2010.

[23] A. R. Alonso, J. Sebastian, D. G. Lamar, M. M. Hernando, and A. Vazquez, "An overall study of a dual active bridge for bidirectional dc/dc conversion," in *Proc. 2010 IEEE Energy Convers. Congr. Expo.*, 2010, pp. 1129–1135.

[24] B. Zhao, Q. Song, W. Liu, G. Liu, and Y. Zhao, "Universal high-frequency-link characterization and practical fundamental-optimal strategy for dual-active-bridge dc-dc converter under PWM plus phase-shift control," *IEEE Trans. Power Electron.*, vol. 30, no. 12, pp. 6488–6494, Dec. 2015.
[25] C. Wang, G. Sha, H. Cheng, and Q. Deng, "Unified phasor analytical method for dual-active-bridge dc/dc converter under phase-shift control," in *Proc. 2016 IEEE 8th Int. Power Electron. Motion Control Conf.*, 2016, pp. 348–355.
[26] W. Choi, K. M. Rho, and B. H. Cho, "Fundamental duty modulation of dual-active-bridge converter for wide-range operation," *IEEE Trans. Power Electron.*, vol. 31, no. 6, pp. 4048–4064, Jun. 2016.
[27] N. Hou, W. Song, and M. Wu, "Minimum-current-stress scheme of dual active bridge dc-dc converter with unified phase-shift control," *IEEE Trans. Power Electron.*, vol. 31, no. 12, pp. 8552–8561, Dec. 2016.
[28] J. Huang, Y. Wang, Z. Li, and W. Lei, "Unified triple-phase-shift control to minimize current stress and achieve full soft-switching of isolated bidirectional dc/dc converter," *IEEE Trans. Ind. Electron.*, vol. 63, no. 7, pp. 4169–4179, Jul. 2016.
[29] L. Li, *Selected Applications of Convex Optimization*, vol. 103. New York, NY, USA: Springer, 2015.
[30] F. Krismer and J. W. Kolar, "Efficiency-optimized high-current dual active bridge converter for automotive applications," *IEEE Trans. Ind. Electron.*, vol. 59, no. 7, pp. 2745–2760, Jul. 2012.
[31] J. Everts, F. Krismer, J. Van den Keybus, J. Driesen, and J. W. Kolar, "Optimal ZVS modulation of single-phase single-stage bidirectional DAB ac/dc converters," *IEEE Trans. Power Electron.*, vol. 29, no. 8, pp. 3954–3970, Aug. 2014.
[32] A. Tong *et al.*, "Power flow and inductor current analysis of PWM control for dual active bridge converter," in *Proc. 2016 8th Int. Power Electron. Motion Control Conf.*, 2016, pp. 1036–1041.
[33] A. Tong, L. Hang, and G. Li, "Global optimized control strategy of dual active bridge converter controlled by triple-phase-shift modulation scheme and its analysis," *Proc. CSEE*, 2017. [Online]. Available: http://kns.cnki.net/kcms/detail/11.2107.TM.20170331.1513.001.html
[34] L. Corradini, D. Seltzer, D. Bloomquist, R. Zane, D. Maksimović, and B. Jacobson, "Minimum current operation of bidirectional dual-bridge series resonant dc/dc converters," *IEEE Trans. Power Electron.*, vol. 27, no. 7, pp. 3266–3276, Jul. 2012.

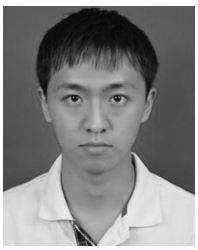

Anping Tong (S'16) received the B.S. degree in electrical engineering from the School of Electrical Engineering, Xi'an Jiaotong University, Xi'an, China, in 2015. He is currently working toward the Ph.D. degree in the School of Electronic Information and Electrical Engineering, Shanghai Jiaotong University, Shanghai, China.

His current research interests include bidirectional isolated dc–dc converters, topology, model, and control of power electronic systems.

Lijun Hang (M'09) received the B.S. and Ph.D. degrees in electrical engineering from Zhejiang University, Hangzhou, China, in 2002 and 2008, respectively.

From 2008 to 2011, she was a Postdoctoral Researcher with Zhejiang University. From 2011 to September 2013, she was a Research Assistant Professor with CURENT, University of Tennessee, Knoxville, TN, USA. She is currently an Associate Professor in the Department of Electrical Engineering, Shanghai Jiao Tong University, Shanghai, China. She has authored or co-authored more than 80 published technical papers. Her research interests include digital control of power electronics for grid connected converters, converters for microgrid, and renewable energy.

Guojie Li (M'09–SM'12) received the B.E. and M.E. degrees in electrical engineering from Tsinghua University, Beijing, China, in 1989 and 1993, respectively, and the Ph.D. degree in electrical engineering from the School of Electrical and Electronic Engineering Nanyang Technological University, Nanyang, Singapore, in 1999.

He was an Associate Professor in the Department of Electrical Engineering, Tsinghua University. He is currently a Professor in the Department of Electrical Engineering, Shanghai Jiao Tong University, Shanghai, China. His current research interests include ac/dc power system analysis and control, wind and PV power control and integration, and DAB control.

Xiuchen Jiang received the B.E. degree in high voltage and insulation technology from the Shanghai Jiao Tong University, Shanghai, China, in 1987, the M.S. degree in high voltage and insulation technology from Tsinghua University, Beijing, China, in 1992, and the Ph.D. degree in electric power system and automation from the Shanghai Jiao Tong University, in 2001.

Currently, he is a Professor in the Department of Electrical Engineering, Shanghai Jiao Tong University. His research interests include electrical equipment online monitoring and condition-based maintenance and automation.

Shenyu Gao received the B.E. degree in electrical engineering and the M.E. degree in economic management from Tsinghua University, Beijing, China, in 1989 and 1991, respectively.

He is currently a Deputy General Manager in Nanjing Power Supply Company, State Grid Jiangsu Electric Power Company, Nanjing, China. His research interests include planning, operation, and dispatch of power grids.